Title

14.8% Quantum Efficient Gallium Phosphide Photocatalyst for Hydrogen Evolution

Permalink

https://escholarship.org/uc/item/0f03361v

Journal

Journal of the American Chemical Society, 146(11)

ISSN

0002-7863

Authors

Becker, Kathleen

Xiao, Chengcan

Assavachin, Samutr

et al.

Publication Date

2024-03-20

DOI

10.1021/jacs.3c14545

Peer reviewed

Article

14.8% Quantum Efficient Gallium Phosphide Photocatalyst for Hydrogen Evolution

Kathleen Becker, Chengcan Xiao, Samutr Assavachin, Anna Kundmann, and Frank E. Osterloh*

Read Online

ACCESS | Metrics & More | Article Recommendations | Supporting Information

ABSTRACT: Gallium phosphide is an established photoelectrode material for H_2 or O_2 evolution from water, but particle-based GaP photocatalysts for H_2 evolution are very rare. To understand the reasons, we investigated the photocatalytic H_2 evolution reaction (HER) of suspended n-type GaP particles with iodide, sulfite, ferricyanide, ferrous ion, and hydrosulfide as sacrificial electron donors, and using Pt, $Rh_yCr_{2-y}O_3$, and Ni_2P HER cocatalysts. A record apparent quantum efficiency of 14.8% at 525 nm was achieved after removing gallium and oxide charge trapping states from the GaP surface, adding a Ni_2P cocatalyst to reduce the proton reduction overpotential, lowering the Schottky-barrier at the GaP−cocatalyst interface, adjusting the polarity of the depletion layer at the GaP−liquid interface, and optimizing the electrochemical potential of the electron donor. The work not only showcases the main factors that control charge separation in suspended photocatalysts, but it also explains why most known HER photocatalysts in the literature are based on n-type and not p-type semiconductors.
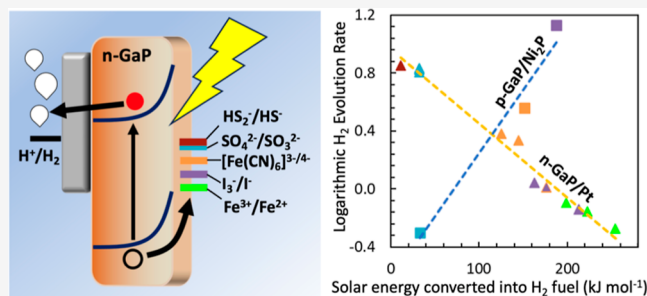
INTRODUCTION

Photocatalytic overall water splitting is a promising pathway to solar hydrogen fuel.[1−6] The best known single-absorber photocatalyst based on $SrTiO_3$ reaches nearly 100% quantum efficiency at 350−360 nm,[7] and the best known particle tandem, $Rh_yCr_{2-y}O_3$−Rh,La/$SrTiO_3$/Mo/$BiVO_4$, achieves a quantum efficiency of 30% at 419 nm.[8] However, the solar-to-hydrogen (STH) efficiencies of both photocatalysts are still low (0.65−1.1%) and fundamentally limited by the large band gaps of the absorbers (3.2 eV for $SrTiO_3$ and 2.3 eV for Rh,La/$SrTiO_3$), and by their low absorptivity in the visible region of the solar spectrum.[9] Because STH efficiency is controlled mainly by the light-harvesting ability of the light absorber,[10] improved photocatalysts require semiconductors with smaller band gaps.[11,12] Main group element compounds are the most promising candidates for such photocatalysts because of their superior electronic properties and because their conduction band edges are sufficiently reducing for protons.[13] However, for reasons not entirely clear, the number of main group element photocatalysts for the hydrogen evolution reaction (HER) is very small compared to many transition metal-based photocatalysts that have been discovered over the years.[14−16] Examples of main group element photocatalysts for HER include C_3N_4,[17] GaN,[18] InGaN,[19] SnS,[20] Si,[21] Ge_3N_4,[22,23] black phosphorus,[24] InP,[25] and Bi_2S_3.[26]

GaP is a main group element semiconductor with a zinc-blend crystal structure and a conduction band edge approximately −1.25 V relative to the proton reduction potential.[27,28] Based on its 2.3 eV band gap,[27] a theoretical

STH of 12% is possible with this material. Indeed, high-performing GaP photoelectrodes[29] have been described for many reactions, including chalcogenide oxidation,[30] water oxidation (with TiO_2 protection layer),[31,32] hydrogen evolution,[33−37] CO_2 reduction,[38,39] methyl viologen[40] and ferrocene reduction.[41] In contrast, demonstrations of GaP particle photocatalysts for HER are rare and are riddled with low activity. In their 2011 paper, Sun et al. confirmed submicromolar but steady H_2 evolution from an irradiated suspension of Pt-decorated GaP nanowires under visible light illumination, and using methanol as electron donor.[42] In 2019, we reported photocatalytic HER with GaP particles obtained from a p-GaP wafer. Using iodide as electron donor, the Ni_2P-modified GaP particles achieved a H_2 evolution activity of 13.5 μmol h^{-1} under visible light illumination.[43] Among other causes, the low activity was attributed to the inverted polarity of the p-GaP space charge region (SCR) at the solid−liquid interface (Figure 1a).

Because the electric field associated with the built-in potential V_{bi} guides photoholes away from the p-GaP−liquid interface, the oxidation of the redox couple in the electrolyte
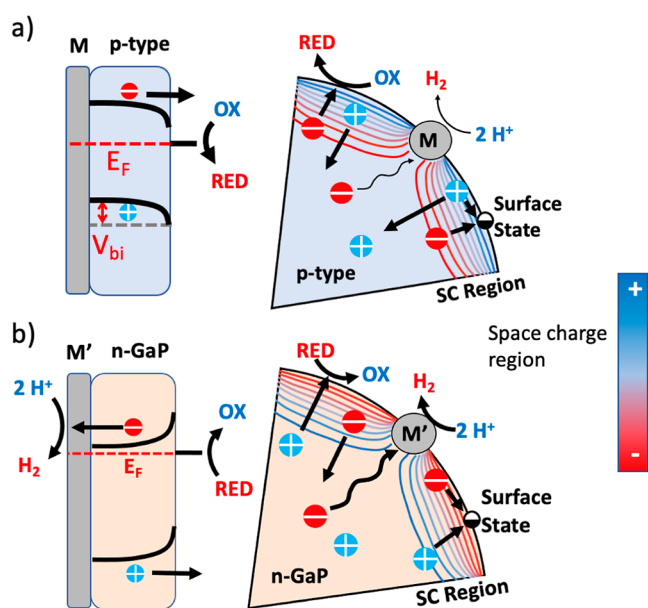
Figure 1. Band bending, charge separation, and surface recombination in illuminated (a) p-type and (b) n-type GaP/M photocatalysts in contact with a sacrificial electron donor (M, M′: HER cocatalysts). Ohmic contacts are assumed at the GaP/metal contacts, and band bending is controlled by the built-in potential at the GaP−liquid contacts. Shown also are the Fermi level (E_F), built-in potential (V_{bi}), and the space charge region (SCR).

becomes difficult. Based on this model, we hypothesize here that greatly improved HER activity should occur with n-GaP particles. The electric field in the depletion layer at the n-GaP/liquid interface has a reversed polarity (Figure 1b) and therefore n-GaP should function as a photoanode for the oxidation of the sacrificial donor. The electrons generated by the process can reach the cocatalyst by diffusion, allowing the HER to occur.

In this work, we confirm this hypothesis with n-GaP particles derived from a commercial S/GaP wafer. The optimized photocatalyst evolves H_2 at 14.8% apparent quantum efficiency (AQE) at 525 nm. This record performance is possible after the removal of charge trapping defects at the n-GaP surface, after the identification of a suitable HER cocatalyst, and after selecting $NaSH/Na_2SO_3$ as the sacrificial electron donor. We also find that the HER rate depends strongly on the electronic properties of the SCR-cocatalyst contact and on the reducing power of the hole scavengers. These observations improve our understanding of how Schottky junctions control charge separation and how the overall reaction energetics drive H_2 evolution. Importantly, the findings explain why most HER photocatalysts in the literature are based on n-type semiconductors rather than p-type materials. This will aid the search for new small band gap photocatalysts for HER.

■ RESULTS AND DISCUSSION

Gallium phosphide particles were obtained as brown or orange powders by mechanical grinding of a commercial n-type sulfur-doped GaP wafer (Figure 2a,b). Based on scanning electron microscopy (SEM) (Figures 2c and S1), the particles are shaped irregularly without distinguishable facets and poly-disperse with an average size of 550 nm. The powder X-ray diffraction pattern (Figure 2d) of the GaP powder matches the zinc blende GaP standard (PDF #00-12-0191) with no
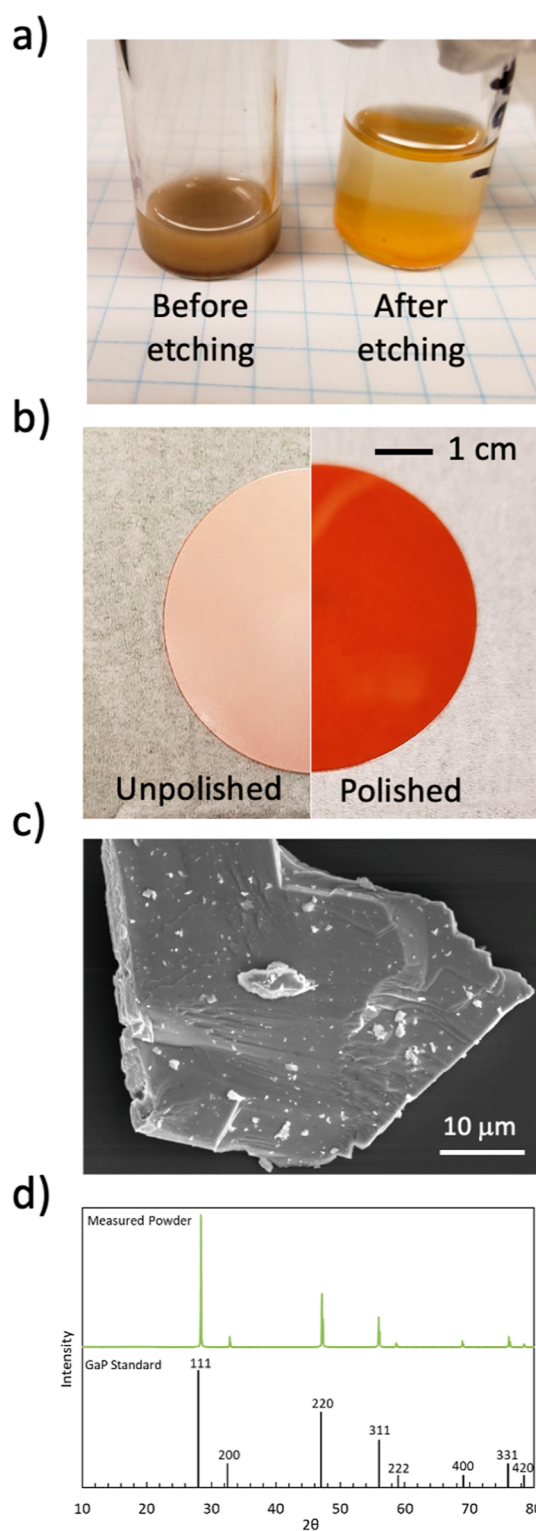

Figure 2. (a) Photos of n-GaP powder suspended in ethanol before and after etching. (b) Photos of the rough and polished sides of the n-GaP wafer. (c) Scanning electron micrograph of a single n-GaP particle obtained from a S-doped GaP wafer and (d) XRD patterns.

impurity phases present. While mechanical grinding of semiconductor wafers is rarely used to obtain photocatalyst particles,[43] previous works have demonstrated wafer etching as a pathway to achieve high surface area photoelectrodes.[40,44]

Diffuse reflectance optical absorption spectra of the two sides of the GaP wafer and of the derived powder are shown in

Figure 3. For the wafer, the spectra reveal an optical absorption onset at 2.16 eV, in the range of the reported optical band gaps
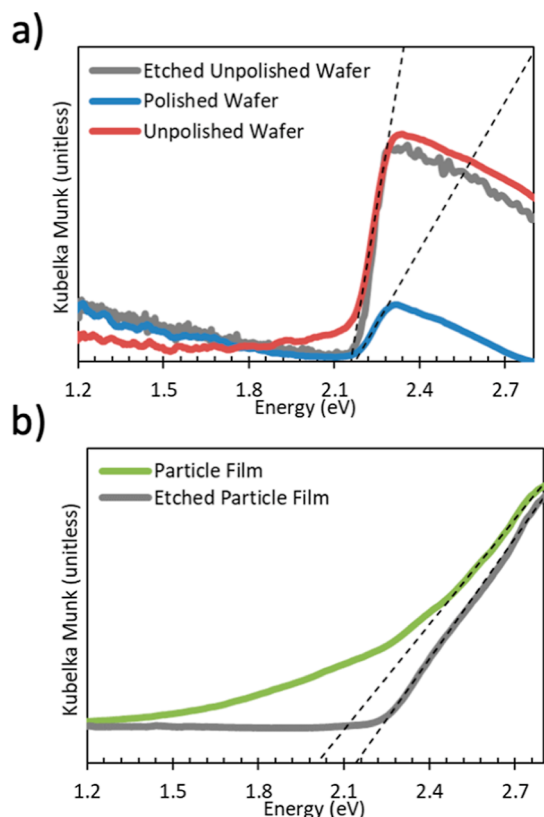
Figure 3. Kubelka−Munk diffuse reflectance spectra of the (a) n-GaP wafer and (b) n-GaP powder. The KM signal of the polished wafer is reduced by the specular reflection on the smooth surface.

(2.1−2.3 eV) for the material.[27,30,45,46] Here, the weaker diffuse reflectance signal for the polished side is due to specular reflection. The spectra also show a very broad absorption at 1.2 eV, which can be attributed to the excitation of free conduction band electrons.[46] The free carriers result from the ionization of S/S^{2-} donor states located 0.107 eV below the GaP conduction band.[27]

In the GaP powder, the main absorption onset is shifted to 1.2 eV, approximately 1 eV below the band gap. The sub-band gap absorption is attributed to states formed during surface oxidation of the GaP powder. Earlier photoluminescence studies[46,47] place O/O^{2-} defects in GaP 0.897 eV below the conduction band edge. These defects are responsible for the brown color of the GaP powder (Figure 3a). Indeed, etching of the GaP powder in piranha acid completely removes the defect absorption in Figure 3b and changes the color of the powder from brown to orange. Etching does not significantly change the particle morphology but causes small pits and trenches to appear on the surface of the larger particles (Figure S1c,d).

To assess the ability of n-GaP to generate a photovoltage under illumination, vibrating Kelvin probe surface photovoltage (VKP-SPV) spectra were recorded on the unpolished side of the as-received wafer. In VKP-SPV, the contact potential difference (CPD) of the wafer is measured in a contactless way with a vibrating, semitransparent gold Kelvin probe.[48] The SPV signal represents the change of the CPD, SPV = CPD (light) − CPD (dark), resulting from light-induced charge separation. It provides an estimate of the

photovoltage of the sample, that is the difference of the electrochemical potentials of the majority and minority carriers at the sample surfaces.[49−51] SPV spectra are shown in Figure 4a together with the logarithmic plot of the xenon arc lamp light intensity. For all samples, negative SPV signals are observed (electrons move away from the Kelvin probe), in agreement with charge separation within the electron depletion layer at the n-GaP surface, as shown in Figure 4b. Analogously, previous SPV measurements on p-GaP have yielded positive SPV signals, due to the opposite polarity of the depletion layer.[43] For n-GaP, the maximum SPV is attained at 3.0 eV, where GaP absorbs light, and the light intensity from the Xe-light source reaches a second a maximum. At higher photon energies, the SPV signal is reduced by the decreasing light intensity of the Xe lamp.

For the etched wafer, the SPV signal begins at 2.06 eV and is assigned to the band gap excitation of GaP. The 0.1 eV deviation from the band gap value in Figure 4a is attributed to Urbach tail states at the GaP surface and near the band edges. These states are detected by SPV, due to its greater sensitivity compared to UV/vis spectroscopy. For the as-received wafers, the photovoltage onset occurs much earlier and is attributed to the excitation of surface defects, as shown in Figure 4b. Based on the 1.3 eV photoonset, the states are located 1.3 eV below the GaP conduction band edge. To identify the chemical origin of the defects, two types of surface treatments were applied to freshly etched wafers. In one experiment, the etched wafer was heated to 600 °C in air for 6 h to create a surface oxide layer. X-ray photoelectron spectroscopy (XPS) survey spectra of the oxidized wafer confirm that this surface treatment causes oxidation of the wafer and leads to increased oxygen and reduced phosphorus content relative to the etched wafer (Figure S2 and Table S3).

The SPV spectrum of the oxidized wafer is also shown in Figure 4a. It contains an increased SPV signal at 3.0 eV, but the sub-band gap signal in the 1.4−1.7 eV region is weaker than in the as-received wafer. This suggests that surface oxides are not responsible for the 1.4 eV photovoltage signal, but instead produce a separate SPV feature at photon energies above 1.8 eV. These states also increase the SPV signal at 3.0 eV by pinning the Fermi level near the O/O^{2-} energy (Figure 4b), which leads to increased band bending. As expected, 5 min of piranha etching of the oxidized wafer restores the SPV spectrum of the original etched wafer.

In a separate experiment, a thin layer of metallic gallium at 30 °C was painted onto the surface of the freshly etched n-GaP (photo in Figure S4). According to XPS, this increases the Ga/P ratio to 2.2 (Table S3) and adds a Ga(0) population at 17.72 eV as the right shoulder to the existing Ga(3+) states of the etched wafer at 19.70 eV[52,53] (Figure 4c and Table S5). The peak assignment of metallic Ga(0) is based on the 1.98 eV energy difference between the right shoulder and the major peak from Ga(3+).[54] The SPV spectrum of the Ga(0) treated n-GaP wafer (Figure 4a) closely resembles the spectrum of the as-received wafer. This confirms that Ga(0) surface states are responsible for the sub-band gap SPV signal via excitation of electrons into the GaP conduction band, as shown in Figure 4b. Based on the 1.3 eV photoonset, the Ga(0) states are located 1.3 eV below the conduction band at +0.1 V vs relative hydrogen electrode (RHE). The Ga(0) states also increase of the photovoltage signal at 3.0 eV, but not as much as the O/O^{2-} states because the Ga(3+/0) potential is more reducing. In the as-received wafer, surface Ga(0) can form by electron
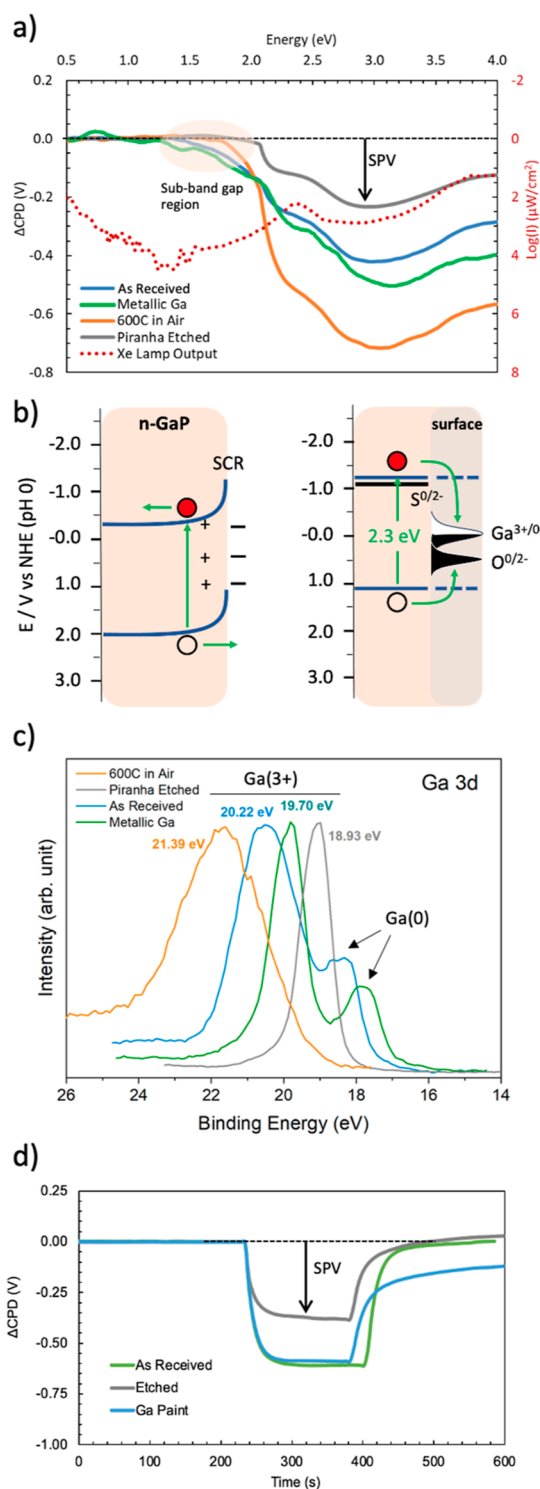
Figure 4. (a) SPV spectra of the unpolished side of the n-GaP wafer before and after surface treatments. The logarithm of the light intensity is shown as dotted line. Above 2.5 eV, the SPV spectra are modulated by the light emission profile of the Xe-light source. (b) Band energy diagrams for n-GaP showing photochemical charge separation and position of defect states. Band edge positions from Chen and Wang.[28] (c) XPS fine structure of n-GaP wafers (Ga region). Spectra are normalized based on the strongest peak. Numerical values are in Table S3 and S5. (d) SPV signal under temporal 405 nm illumination.

transfer from the GaP wafer (E_F = −1.1 V vs RHE) into empty Ga(+3) surface states. Indeed, XPS (Figure 4c) confirms the presence of both Ga(3+) and Ga(0) on the as-received wafer. In the oxidized wafer, on the other hand, all gallium is present in the form of Ga_2O_3 or $GaPO_m$ (m = 3−4), based on the Ga^{3+}−O−P $3d_{5/2}$ peak at 21.39 eV.[55]

To further evaluate the effect of the surface states on the charge carrier dynamics of the GaP wafer, SPV signals were recorded under temporal 405 nm LED illumination (Figure 4d). This produces SPV signals of magnitude comparable to the data in Figure 4a. The photovoltage forms reversibly and quickly, indicating good carrier mobility, as is typical for what was previously observed for GaAs, silicon, and GaN.[56−58] For the as-received and etched GaP wafers, the photovoltage signal forms on the 10−15 s time scale and decays on the 20 s time scale. For the gallium-treated wafer, the decay is much slower (55 s), and 22% of the photovoltage is retained after 200 s. That shows that the Ga(0)-states on the wafer surface can trap photoholes, as shown in Figure 4b.

Next, to evaluate the ability of n-GaP particles to function as a photocatalyst for H_2 evolution, 50 mg of n-GaP powder was suspended in 50 mL of aqueous 0.05 M KI in 0.1 M phosphate buffer at pH 7.2 and irradiated with visible light. Potassium iodide was chosen as a mild sacrificial electron donor because it works well with a p-GaP HER photocatalyst.[43] As can be seen in Figure 5a, H_2 is evolved at a small but steady rate of 0.67 μmol/h. When the n-GaP particles are etched prior to illumination, the H_2 concentration increases to 1.12 μmol/h. This shows that the removal of the O and Ga surface states boosts the photocatalytic activity. This agrees with the well-established fact that states in the middle of the band gap promote recombination of carriers by trapping electrons and holes.[7,59,60] This reduces the steady-state hole concentration under illumination and, with it, the driving force for the photoelectrochemical reaction.

Because it is known that GaP has a substantial kinetic overpotential for the HER,[61] further activity increases are expected from adding a HER cocatalyst. Accordingly, Pt, $Rh_yCr_{2−y}O_3$, or Ni_2P cocatalysts were attached to the GaP particles by photodeposition or impregnation, as described in the Experimental Section. These materials have been shown to reduce protons at low overpotentials.[62−65] Transmission electron microscopy (TEM) images in Figure S6 show that the cocatalysts are randomly distributed on the GaP surface. As can be seen in Figure 5b, etched n-GaP particles loaded with Pt, $Rh_{2−y}Cr_yO_3$, and Ni_2P evolve H_2 at 7.69, 8.26, and 37.90 μmol/h, respectively, approximately 7−34 times faster than without cocatalysts (data in Figure S7). Again, H_2 evolution rates of the nonetched GaP particles are much lower. This is a result of recombination at the photohole trapping Ga(+3/0) surface states, as seen in the photovoltage spectra.

The photocatalytic experiments show that Ni_2P outperforms Pt and $Rh_{2−y}Cr_yO_3$ as HER cocatalyst. This disagrees with the hydrogen evolution overpotentials of the materials which increase in order of Pt < Ni_2P < $Rh_{2−y}Cr_yO_3$, i.e., Pt is a better HER catalyst than Ni_2P.[62−66] Instead, the reactivity trend can be explained with the Schottky-junction model in Figure 5c. Based on the known work functions of Pt (5.64 eV)[67] and Ni_2P (4.69 eV),[68] significant Schottky barriers of 2.24 and 1.29 eV, respectively, are expected at the n-GaP (E_F = 3.4 eV)-cocatalyst interfaces. Indeed, for n-GaP/Pt a Schottky barrier of 1.5 eV has been measured previously.[69] These barriers prevent electron transfer from n-GaP to the cocatalyst and thus
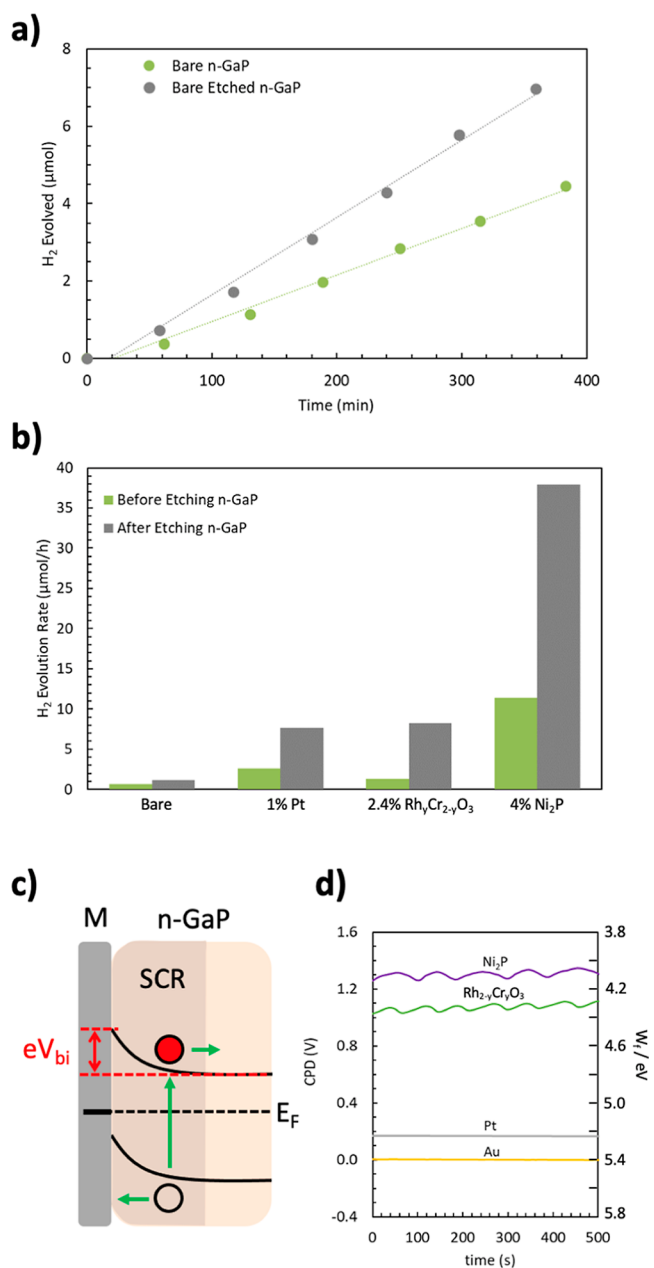
Figure 5. (a) H_2 evolution data from n-GaP powder in 50.0 mL of 0.05 M KI in 0.10 M phosphate buffer at pH 7.2 under visible light (λ > 400 nm, 300 W Xe arc lamp, 380−450 mW cm^{-2} irradiance at the flask). (b) Summary of H_2 evolution data for bare, 1% Pt, 2.4% $Rh_yCr_{2-y}O_3$, and 4% Ni_2P-loaded photocatalysts using etched and nonetched GaP particles. Measured data are shown in Figure S7 and Table S8. (c) Schottky junction at the GaP−cocatalyst (M) interface. To reach the cocatalyst M, photogenerated electrons need to overcome the barrier eV_{bi}, where V_{bi} is the built-in potential [E_F (M) − E_F (GaP)]. (d) CPD values (relative to gold, measured in a vacuum) for $Rh_{2-y}Cr_yO_3$ and Ni_2P films and a Pt wire.

inhibit proton reduction. Ni_2P has the smallest barrier with GaP, and therefore, electron transfer to the cocatalyst is fastest and the HER rate is highest. Based on Kelvin probe CPD measurements (Figure 5d), the work function of $Rh_{2-y}Cr_yO_3$ is in between that of Pt and Ni_2P, and therefore, the n-GaP/$Rh_{2-y}Cr_yO_3$ Schottky barrier is of intermediate height. This data agrees well with the reactivity trend seen in Figure 5b, confirming that the Schottky junction at the GaP−cocatalyst

interface is a limiting factor for HER. An alternative explanation for the lower performance of the n-GaP/Pt photocatalyst is an increased electron−hole recombination rate at the n-semiconductor/metal interface, as has been observed experimentally for n-GaInP$_2$/Pt.[70]

To further optimize hydrogen evolution from the photocatalysts, irradiation experiments were conducted with different sacrificial electron donors, incl. iodide (I^-), ferrous ion (Fe^{2+}), sulfite (SO_3^{2-}), hydrosulfide (HS^-), and hexacyanoferrate ($Fe(CN)_6^{4-}$). Because electrochemical reactions are driven by the charge transfer thermodynamics,[71] the rate of the overall photocatalytic process shown in Figure 6a is expected to be a function of the redox potential of the sacrificial electron donor. Indeed, this is confirmed experimentally. Figure 6b shows a plot of the measured H_2 evolution rates (Figure S9) versus the pH-corrected electrochemical potential (RHE) of the donors (full cell potentials in Table S10). It can be seen that H_2 rates are a direct function of the reducing power, with highest values (~7.06 μmol/h) seen for Na_2SO_3 and Na_2S and lowest values for KI and $FeSO_4$, due to the less reducing electrochemical potentials of the latter. Identical H_2 evolution rates are observed for KI at pH 6.2 and HCF at pH 9.4 because the redox potentials of these two donors are equal (0.91 V vs RHE). This confirms that the reducing power of the electron donor is the main determinant of the H_2 evolution rate.

The redox potentials of the $HCF^{3-/4-}$, I_3^-/I^-, and $Fe^{3+/2+}$ couples are pH-independent of the NHE scale but not on the pH-dependent RHE scale. As a result, the HER rates for these couples increase with decreasing pH. The SO_4^{2-}/SO_3^{2-} redox couple, on the other hand, has the same 59 mV pH^{-1} dependence as the RHE, so the two pH dependences cancel out, and similar HER rates (6.6 μmol/h) are observed at all 3 pH conditions. The results in Figure 6 confirm that the H_2 evolution kinetics with the n-GaP/Pt photocatalyst are controlled by the Gibbs free energy change (ΔG_R) of the overall photocatalytic reaction, as shown in eqs 1 and 2.

$$2\,\text{Red} + 2\text{H}^+ \rightarrow \text{H}_2 + 2\,\text{Ox} \tag{1}$$
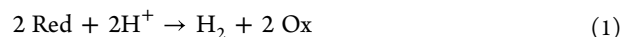
$$\Delta G_R = -2F\,[E^0(\text{H}^+/\text{H}_2) - E^0(\text{Ox}/\text{Red})] \tag{2}$$

$$\Delta G^{\ddagger} = \alpha \Delta G_R + \beta \tag{3}$$

$$k_{H_2} = (k_B T/h)\,\exp(-\Delta G^{\ddagger}/RT) \tag{4}$$

Here, RED and OX are the reduced and oxidized forms of the sacrificial reagent, and F is the Faraday constant. Assuming a linear free energy relationship (eq 3) between the Gibbs free energy change (ΔG_R) and the Gibbs free energy of activation $\Delta G^{\ddagger}$ (α and β are constants),[71] and using the Eyring eq 4 for the kinetic rate constant k_{H_2}, it can be seen that the logarithmic hydrogen evolution rate should have a linear dependence on the driving force for the overall reaction (at constant pH). Indeed, a plot of $\log_{10}(r_{H_2})$ versus ΔG_R is linear (orange fit in Figure 6c), confirming the validity of this model. Small deviations from linearity are attributed to the effect of the proton concentration on the electron transfer rate, which is not captured in eqs 3 or 4. Figure 6c also shows that the reaction is endergonic (ΔG_R is positive) for all of the electron donors. This means that H_2 evolution results from the net conversion of photochemical energy into Gibbs free energy (eq 1), as wanted for a fuel-forming process.[72] The highest rates are seen for sulfide because it is the most reducing electron donor (E^0 =
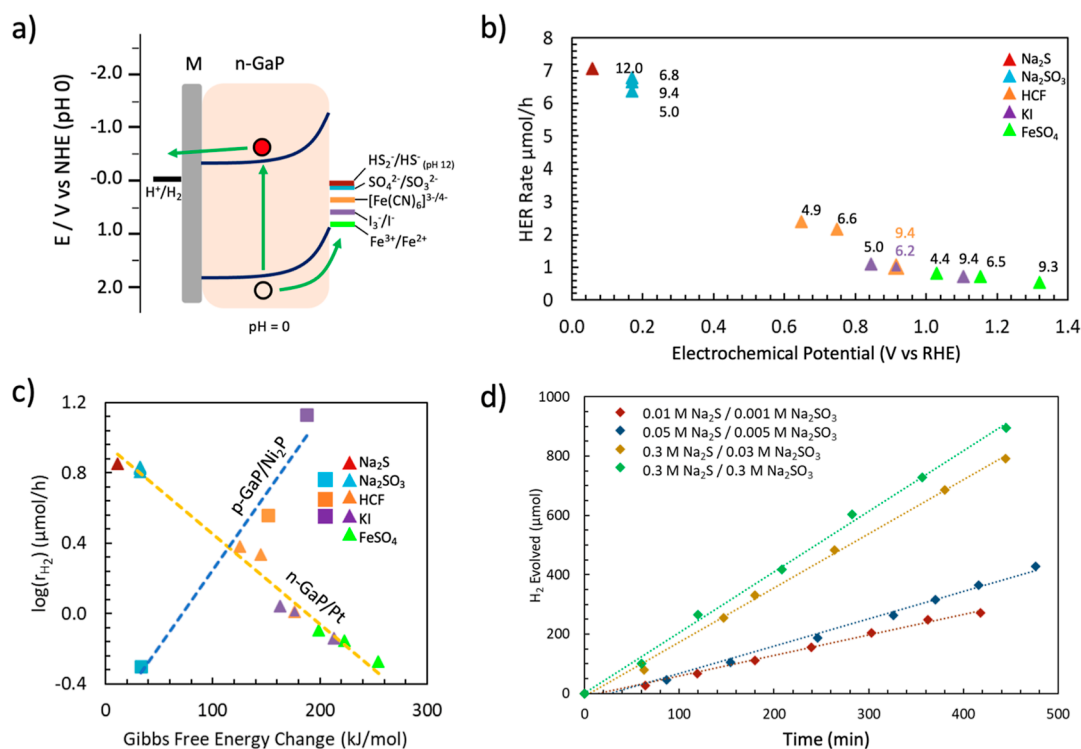
Figure 6. (a) Energy diagram of n-GaP photocatalyst in the presence of sacrificial electron donors. The E^0 for HS_2^-/HS^- is shown at pH 12 because E^0 is not defined at pH 0. (b) Measured HER rates vs the electrochemical potential of the sacrificial donors at various pH values (labels in the plot). Experimental data is shown in Figure S9 and numerical data in Table S10. (c) The plot of the logarithmic hydrogen evolution rate of n-GaP/Pt and p-GaP/Ni$_2$P versus reaction Gibbs energy change ΔG_R. Note that ΔG_R is positive for all conditions, corresponding to a thermodynamically forbidden (endergonic) process. Data for p-GaP/Ni$_2$P from Zhao et al.[43] (d) H$_2$ evolution from 4%-loaded Ni$_2$P/n-GaP (etched) in 50.0 mL aqueous sulfide/sulfite solution under visible light (λ > 400 nm, 300 W Xe arc lamp, estimated irradiance at the flask 380−450 mW cm^{-2}). Data is listed in Table S11.

0.055 V vs RHE at pH 12) in the series. Remarkably, the reactivity trend (blue fit) for the earlier reported p-GaP/Pt HER photocatalysts is the opposite of that for n-GaP/Ni$_2$P photocatalyst.[43] For the p-GaP/Ni$_2$P catalyst, the H$_2$ evolution rate decreases with increasing the driving force of the reaction ΔG_R (Figure 6c). This is due to the dominating influence of the SCR at the p-GaP/liquid contact on charge separation. Because the polarity of the SCR in p-GaP is inverted (Figure 1a), it impedes hole transfer from p-GaP to the sacrificial donors and prevents the capture of electrons needed for proton reduction. According to SPV measurements, hole-transfer barrier heights (V_{bi}) for the p-GaP/electrolyte interface increase in the order of KI (0.25 eV), HCF (0.37 eV), and Na$_2$SO$_3$ (0.45 eV).[43] This agrees with the prediction of the Schottky model, according to which the barrier $V_{bi} = E^0$ (Ox/red) − E_F (GaP) grows as the sacrificial electron donors become more reducing (Figure 1a). For n-GaP, on the other hand, the SCR does not introduce a hole transfer barrier, and the rate of the HER is instead controlled by the linear free energy relationship in eq 3.
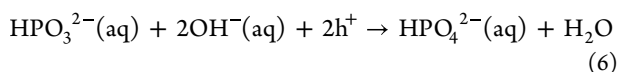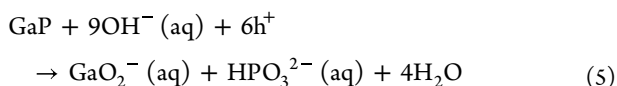
The model in Figure 1 not only explains the data for n-GaP studied here but can rationalize the established dominance of n-type over p-type photocatalysts for the HER.[3,73] For p-type photocatalysts, the polarity of the semiconductor−liquid junction prevents electron collection from the sacrificial donor in solution, which limits hydrogen evolution. When p-type semiconductors are used as HER materials, this problem is usually avoided by moving electrons into the semiconductor through a solid−solid contact. This can be done by interfacing

the p-type semiconductor with an electrode support, for example in p-CuGa$_3$Se$_5$ photocathodes,[74] or with a n-type semiconductor, as in the Ru/SrTiO$_3$/Rh/BiVO$_4$ tandem.[75] Alternatively, the semiconductor−liquid junction hole transfer barrier is reduced by raising the semiconductor Fermi level through alloying with non-p-type semiconductors, as in (ZnSe)$_{0.5}$(CuGa$_{2.5}$Se$_{4.25}$)$_{0.5}$.[76] However, stand-alone p-type photocatalysts for HER will always be limited by the incorrect polarity of the solid−liquid junction in Figure 1a, which prevents electron collection from the solution phase.

The data in Figure 6 suggest that a record performance may be achieved with the n-GaP/Ni$_2$P catalyst by choosing hydrosulfide as sacrificial donor with the most negative standard reduction potential. Accordingly, H$_2$ evolution experiments were repeated with n-GaP/Ni$_2$P (etched) in Na$_2$S solutions containing 10% (mol) Na$_2$SO$_3$. Sulfite is added to convert formed polysulfide into thiosulfate, thereby reducing light shading from the former.[77] As seen in Figure 6d, H$_2$ is evolved linearly in all cases, and the rates increase with an increasing sacrificial donor concentration. The highest rate of 123 μmol/h is observed for a solution containing 0.3 M Na$_2$S and 0.3 M Na$_2$SO$_3$. When the experiment is repeated under 525 nm LED illumination, H$_2$ is evolved at a rate of 11.8 μmol h^{-1} (Figure S12 and Table S13), corresponding to an AQE of 14.8%. For n-GaP particles loaded with Rh$_{2-y}$Cr$_y$O$_3$, Pt, and bare n-GaP, AQEs are 6.3, 5.2, and 0.5%, respectively, lower than those of n-GaP particles loaded with Ni$_2$P, as expected, and following the previously observed trend. These

are the highest reported AQEs for H_2 evolution from GaP photocatalyst particles.[42,43,78−80]

To evaluate the long-term stability of the n-GaP/Ni$_2$P photocatalyst in sulfide/sulfite, sequential irradiation experiments were conducted at 6 h intervals. Over the 18 h period (Figure S7d) 1.4 mmol of H_2 are evolved, corresponding to a turnover number of 2.8 for the photocatalyst. This suggests a catalytic process. However, as can be seen from the plot, the rate decreases by approximately half after each experiment, until it is only 31% of the original rate. This shows that the GaP/Ni$_2$P photocatalyst is not stable under the reaction conditions. Photocorrosion is a known problem of n-GaP in aqueous solutions.[30,81] In the absence of stabilizing agents, GaP undergoes photoanodic conversion into either Ga(3+) and phosphoric acid (in acidic solution), or GaO_2^- and elemental phosphor (in alkaline solution), with P undergoing further oxidation.[81,82] Indeed, when a proton-decoupled ^{31}P NMR spectrum (Figure S14) was recorded on the supernatant after an 18 h illumination period, a mixture of hydrogen phosphate (HPO_4^-) and phosphite (HPO_3^{2-}) is observed. Phosphite is formed by direct photocorrosion of GaP (eq 5), whereas hydrogen phosphate is formed by photocatalytic oxidation (eq 6) under the air-free conditions of the reaction.

$$GaP + 9OH^-\,(aq) + 6h^+$$
$$\rightarrow GaO_2^-\,(aq) + HPO_3^{2-}\,(aq) + 4H_2O \qquad (5)$$

$$HPO_3^{2-}(aq) + 2OH^-(aq) + 2h^+ \rightarrow HPO_4^{2-}(aq) + H_2O \qquad (6)$$

These side reactions limit the usability of the n-GaP/Ni$_2$P photocatalytic system for the large-scale photocatalytic production of H_2. Greater stability might be achievable by using selenide or telluride ions as alternative electron donors.[30]

CONCLUSIONS

In summary, we demonstrate photocatalytic H_2 evolution from Ni$_2$P-modified n-GaP particles with an AQE of 14.8% at 525 nm, 2 orders of magnitude higher than previous reports. The performance is a result of systematic optimization of junctions at the n-GaP−liquid and n-GaP−cocatalyst interfaces, removal of Ga(3+/0) and O(0/2−) surface defects, and adjustment of the redox potential of the sacrificial electron donor. The work shows that the correct polarity of the solid−liquid junction is essential to achieving hydrogen evolution with a semiconductor photocatalyst. In n-GaP photocatalysts, the depletion layer guides photoholes toward the sacrificial donor while in p-GaP particles the depletion layer moves photoholes away from it, preventing the collection of electrons for proton reduction. This explains the predominance of n-type semiconductors as hydrogen evolution photocatalysts in the literature. The work also reveals the importance of an ohmic contact at the GaP−cocatalyst contact. Pt and Rh$_{2−y}$Cr$_y$O$_3$ cocatalysts with large work functions generate a Schottky barrier with n-GaP that prevents electrons from reaching the cocatalyst. For Ni$_2$P the barrier is the smallest, which explains the higher H_2 evolution activity with this cocatalyst. Also, we find that Ga(3+/0) surface defects reduce the photocatalytic activity by trapping holes, but they can be removed by etching GaP with piranha acid. Furthermore, we show that photocatalytic HER with n-GaP/Pt follows a free energy relationship, i.e. the more reducing the sacrificial donor, the larger the H_2 evolution rate. Notably, all n-GaP/Ni$_2$P systems reported

here generate H_2 under endergonic conditions, resulting in energy storage up to 1.3 eV per converted photon (with Fe^{2+} at pH 9.3). This is relevant to the development of n-GaP-derived tandem photocatalysts for overall water splitting. A side aspect of the free energy relationship is the observed dependence of the H_2 evolution rate on the solution pH. This effect is observed for sacrificial donors with a pH-independent redox potential (Fe^{2+}/Fe^{3+}, $Fe(CN)_6^{3-/4-}$), but not for sulfite, where the pH dependences of the donor and of the proton reduction reaction cancel out. Lastly, phosphate and phosphite are identified by NMR as products of GaP photocorrosion during photocatalysis. Improved stability may be achievable with other sacrificial donors, such as selenide, or by coupling the Ni$_2$P/n-GaP system to a water oxidation catalyst.

EXPERIMENTAL SECTION

N-type gallium phosphide wafers doped with sulfur (0.20−0.125 Ω cm, carrier density 4.5×10^{17}−4.75×10^{17} cm^{-3}) were obtained from EL-CAT Inc. Hydrogen peroxide (30 wt % in H_2O), concentrated sulfuric acid, potassium iodide (99.9%), potassium hexacyanoferrate (ii) (99%), potassium hydroxide (99%), sodium sulfite (98%), sodium sulfide nonahydrate (98%), iron (II) sulfate (99%), bisacetylacetonate nickel (II) (98%, eMolecules), trioctylphosphine (90%), oleylamine (80−90%, Fisher Scientific), dioctyl ether (99%, Fisher Scientific), hexanes (98.5%), chloroform (HPLC grade, Thermo Fisher), ethanol (200 proof), isopropanol (>99%), acetone (99.9%), polyvinylpyrrolidone (MM = 55,000), dihydrogen hexa-chloroplatinate (IV) (99.9%, Alfa Aesar), rhodium(III) chloride (>99%, Fisher Scientific), chromium(III) nitrate nonahydrate (99%, Acros Organics) were used as received. Water was purified using a Nanopure system. Caution: nickel compounds are carcinogenic.

GaP particles were prepared by grinding the commercial wafers for 45 min in an N_2 atmosphere in a glovebox using a mortar and pestle. The resulting powder was stored in a closed container in the dark under N_2. The GaP wafer or the GaP particles were etched in a small beaker containing 3 mL H_2SO_4, 1 mL H_2O_2, and 1 mL H_2O ("piranha acid") at 50 °C for 5 min (particles) or 30 min (wafer). The wafer was washed 5 times with nanopure water to remove excess acid. The particle suspension was diluted to 50 mL of nanopure water after etching and centrifuged at 9000 rpm for 4 min. This was repeated an additional 4 times with 50 mL of water. The etched wafer and particles were dried in the dark under a N_2 flow.

Fluorine-doped tin oxide (FTO) and gold coated glass substrates were cleaned by ultrasonication in acetone for 15 min followed by nanopure water for an additional 15 min. The cleaned substrates were dried at 60 °C for at least 1 h.

Particle films (GaP, Rh$_y$Cr$_{2−y}$O$_3$, or Ni$_2$P) on conductive substrates were fabricated by dispersing 10 mg of the respective powders in 1 mL of ethanol via sonication for 15−30 min. A 0.04 mL aliquot of the suspension was drop-coated onto FTO or Au substrates using a circular mask (38.5 mm^2) made from polyester masking tape, followed by drying under N_2 flow in the dark for 1 h. Subsequent layers were added until the desired thickness was achieved. n-GaP particle films were allowed to dry under N_2 flow in the dark and then annealed under argon for 3 h at 450 °C to achieve electric contact with the substrate.

Ni$_2$P cocatalyst particles of average diameter of 12 nm were prepared via an air-free two-step synthesis.[62,83] All glassware was cleaned and dried overnight in a 60 °C oven before use. In a 50 mL two-necked round-bottom flask equipped with a coil condenser, 0.50 g (2.0 mmol) of Ni(acac)$_2$, 8 mL (25 mmol) of dioctyl ether, 3 mL (9 mmol) of oleylamine, 6 mL (14 mmol) of trioctylphosphine, and a stir bar were combined. The system was purged and refilled with N_2 three times before it was heated to 120 °C with a heating mantle. The system was left under a vacuum to remove water and other impurities with low boiling points. The solution was then heated to 220 °C for 1 h to allow the formation of Ni nanoparticles followed by an increase in temperature to 350 °C for 8+ hours to form Ni$_2$P. The reaction

mixture was then cooled slowly to 200 °C before being removed from the heating mantle and cooled to room temperature. The liquid reaction mixture was transferred into centrifuge tubes and separated by centrifuging at 12,500 rpm for 5 min. The black product was then washed with a 1:4 by volume mixture of hexanes and ethanol 5 times and suspended in 12 mL of pure hexanes via sonication for the ligand exchange reaction. The balanced reaction for the synthesis of the dinickel phosphide is $4Ni(C_5H_7O_2)_2 + H_2NC_{18}H_{37} + 2P(C_8H_{17})_3 \rightarrow 2Ni_2P + 6C_8H_{16} + HNC_{18}H_{36} + 8C_5H_8O_2$.

A 200 mL two-neck round-bottom flask was charged with 125 mL of chloroform containing 1.0 g of polyvinylpyrrolidone. The nanoparticle suspension was added, and the system was purged and refilled with nitrogen 5 times. The flask was heated to 65 °C for 10−12 h using an oil bath. Once cooled to room temperature, the product was centrifuged out after adding twice the volume of acetone (antisolvent) to the reaction mixture. A centrifuge speed of 12,500 rpm was needed to separate the majority of the product from the supernatant. The resulting black powder was washed 5 times with acetone and then dried in a vacuum. The Ni_2P particles were stored in a glovebox until use.

Pt cocatalyst loading: platinum was deposited onto GaP particles by irradiating 200 mg of GaP particles in 100 mL of an aqueous solution of H_2PtCl_6 (1 wt % Pt with respect to GaP) and 20% methanol for 3 h under illumination from an unfiltered 300 W Xe arc lamp. The solid product was isolated by sedimentation and washed three times with nanopure water, followed by drying in vacuum. The resulting powder was stored in a nitrogen-filled glovebox in the dark until use.

$Rh_yCr_{2-y}O_3$ cocatalyst loading: the cocatalyst was deposited by impregnation/calcination as previously reported.[84] In a small beaker, GaP, $RhCl_3 \cdot xH_2O$ (0.5 wt % Rh), $Cr(NO_3)_3 \cdot 9H_2O$ (1 wt % Cr) and 30 mL of nanopure water were mixed and heated in an 80 °C water bath with occasional stirring. The resulting powder was collected after 2 h and heated in air at 350 °C for 1 h.

Ni_2P cocatalyst loading: the Ni_2P cocatalyst was added to 100 mg of n-GaP to achieve ∼4% (mass) loading. The particle mixture was suspended in a few mL of ethanol and sonicated for 15 min to disperse the Ni_2P nanoparticles. Next, the mixture was transferred to a mortar and ground under air until the ethanol evaporated. The fine and uniform powder was transferred into a ceramic boat and annealed under argon flow in a tube furnace. The temperature was held at 450 °C for 3 h to ensure good contact between the Ni_2P and n-GaP particles.

SEM and energy dispersive X-ray spectroscopy (EDX) of GaP samples and particle films on a Au substrate were taken on a Scios DualBeam SEM/FIB instrument. TEM was performed on a FEI L120C TEM with an accelerating voltage of 80 kV.

Powder X-ray diffraction measurements were performed on a Bruker D8 Advance Eco with a Cu Kα radiation source and a monochromatic wavelength of 0.15418 nm. UV−vis diffuse reflectance spectra were recorded on a Thermo Scientific Evolution 220 spectrometer by using dried sample films and white teflon tape as a reference.

XPS measurements were conducted on a Supra XPS spectrometer using an Al Kα source that generate X-rays at 1487 eV and an ultrahigh vacuum (UHV) analytical chamber with a pressure of 10^{-7} mbar. The spectra were electrostatically corrected based on the position of C 1s (284.6 eV). Baseline simulation of the core-level spectrum was done using the Shirley method.

SPV spectra were measured under vacuum ($\leq 6.0 \times 10^{-4}$ mbar) on wafer pieces. A Besocke gold Kelvin probe was used as the reference electrode. Samples were illuminated with a 300 W xenon lamp. The light was filtered through an Oriel Cornerstone 130 monochromator to obtain spectra in the 0.4−4.0 eV window (scanning from low to high energy). Transient SPV data was collected by illumination with a 405 nm LED. All SPV data is referenced against the CPD value in the dark.

Work function measurements were performed under vacuum using a vibrating gold Kelvin probe reference electrode that was calibrated with a gold-coated glass substrate. Particle films of Ni_2P or

$Rh_xCr_{2-x}O_3$ were provided on gold-coated glass substrates. The Pt work function was measured from a Pt wire electrode that was coiled tightly and flattened to fit under the Kelvin probe.

Photocatalytic HER experiments were performed by suspending 50 mg of GaP particles (or 50 mg of cocatalyst-modified GaP) in 50 mL of 0.05 M electron donor (unless otherwise stated) in a 100 mL round-bottom flask. The reaction flask was purged and refilled with argon 5 times before beginning irradiation. A 300 W Xe arc lamp with a 400 nm long pass filter (0.22 M $NaNO_3$ solution) was used to irradiate the suspension. The lamp intensity was measured to be 380−450 mW cm^{-2} at the surface of the flask by an IL1400BL photometer equipped with a GaAsP detector for 280−660 nm sensitivity range. A mirror behind the sample flask was employed to ensure full illumination, and a fan was used to maintain a constant temperature of 35 °C. The irradiation system was hardwired to a Varian 3800 gas chromatograph with a 60/80 Å molecular sieve column and thermal conductivity detector to identify quantities of H_2, O_2, and N_2 in the flask at various times.

Phosphorus nuclear magnetic resonance (NMR) spectroscopy was performed using a Varian 600 MHz NMR spectrometer and data was analyzed using VnmrJ software. Samples were prepared by centrifuging the solution after HER experiments at 10,000 rpm. The supernatant was then dried using rotary evaporation and resuspended in D_2O. The solution was filtered into an NMR tube and the P-31 NMR was conducted using manual tuning and 32−64 pulses with and without proton decoupling.

■ ASSOCIATED CONTENT

Ⓢ Supporting Information

The Supporting Information is available free of charge at https://pubs.acs.org/doi/10.1021/jacs.3c14545.

> Experimental details, electron micrographs, photos, H_2 evolution data, XPS data, NMR spectra, and H_2 evolution data (PDF)

■ AUTHOR INFORMATION

Corresponding Author

Frank E. Osterloh − *Department of Chemistry, University of California, Davis, California 95616, United States;* ⊙ orcid.org/0000-0002-9288-3407; Email: fosterloh@ucdavis.edu

Authors

Kathleen Becker − *Department of Chemistry, University of California, Davis, California 95616, United States*

Chengcan Xiao − *Department of Chemistry, University of California, Davis, California 95616, United States*

Samutr Assavachin − *Department of Chemistry, University of California, Davis, California 95616, United States*

Anna Kundmann − *Department of Chemistry, University of California, Davis, California 95616, United States;* ⊙ orcid.org/0000-0003-2157-8541

Complete contact information is available at:
https://pubs.acs.org/10.1021/jacs.3c14545

Notes

The authors declare no competing financial interest.

■ ACKNOWLEDGMENTS

■ REFERENCES

(1) Segev, G.; Kibsgaard, J.; Hahn, C.; Xu, Z. J.; Cheng, W.-H.; Deutsch, T. G.; Xiang, C.; Zhang, J. Z.; Hammarström, L.; Nocera, D. G.; Weber, A. Z.; Agbo, P.; Hisatomi, T.; Osterloh, F. E.; Domen, K.; Abdi, F. F.; Haussener, S.; Miller, D. J.; Ardo, S.; McIntyre, P. C.; Hannappel, T.; Hu, S.; Atwater, H.; Gregoire, J. M.; Ertem, M. Z.; Sharp, I. D.; Choi, K.-S.; Lee, J. S.; Ishitani, O.; Ager, J. W.; Prabhakar, R. R.; Bell, A. T.; Boettcher, S. W.; Vincent, K.; Takanabe, K.; Artero, V.; Napier, R.; Cuenya, B. R.; Koper, M. T. M.; Van De Krol, R.; Houle, F. The 2022 solar fuels roadmap. *J. Phys. D: Appl. Phys.* **2022**, *55* (32), 323003.

(2) Takata, T.; Jiang, J.; Sakata, Y.; Nakabayashi, M.; Shibata, N.; Nandal, V.; Seki, K.; Hisatomi, T.; Domen, K. Photocatalytic water splitting with a quantum efficiency of almost unity. *Nature* **2020**, *581* (7809), 411−414.

(3) Fabian, D. M.; Hu, S.; Singh, N.; Houle, F. A.; Hisatomi, T.; Domen, K.; Osterloh, F. E.; Ardo, S. Particle Suspension Reactors and Materials for Solar-Driven Water Splitting. *Energy Environ. Sci.* **2015**, *8*, 2825−2850.

(4) Nishioka, S.; Osterloh, F. E.; Wang, X.; Mallouk, T. E.; Maeda, K. Photocatalytic water splitting. *Nat. Rev. Methods Primers* **2023**, *3* (1), 42.

(5) Nozik, A. J. Photochemical Diodes. *Appl. Phys. Lett.* **1977**, *30* (11), 567−569.

(6) Kudo, A.; Miseki, Y. Heterogeneous Photocatalyst Materials for Water Splitting. *Chem. Soc. Rev.* **2009**, *38* (1), 253−278.

(7) Zhao, Z.; Goncalves, R. V.; Barman, S. K.; Willard, E. J.; Byle, E.; Perry, R.; Wu, Z.; Huda, M. N.; Moulé, A. J.; Osterloh, F. E. Electronic structure basis for enhanced overall water splitting photocatalysis with aluminum doped SrTiO3 in natural sunlight. *Energy Environ. Sci.* **2019**, *12*, 1385−1395.

(8) Wang, Q.; Hisatomi, T.; Jia, Q.; Tokudome, H.; Zhong, M.; Wang, C.; Pan, Z.; Takata, T.; Nakabayashi, M.; Shibata, N.; Li, Y.; Sharp, I. D.; Kudo, A.; Yamada, T.; Domen, K. Scalable water splitting on particulate photocatalyst sheets with a solar-to-hydrogen energy conversion efficiency exceeding 1%. *Nat. Mater.* **2016**, *15*, 611−615.

(9) Han, R.; Melo, M. A., Jr.; Zhao, Z.; Wu, Z.; Osterloh, F. E. Light Intensity Dependence of Photochemical Charge Separation in the BiVO4/Ru-SrTiO3:Rh Direct Contact Tandem Photocatalyst for Overall Water Splitting. *J. Phys. Chem. C* **2020**, *124*, 9724−9733.

(10) Bolton, J. R.; Strickler, S. J.; Connolly, J. S. Limiting and Realizable Efficiencies of Solar Photolysis of Water. *Nature* **1985**, *316* (6028), 495−500.

(11) Maeda, K.; Domen, K. New non-oxide photocatalysts designed for overall water splitting under visible light. *J. Phys. Chem. C* **2007**, *111* (22), 7851−7861.

(12) Xiao, J.; Hisatomi, T.; Domen, K. Narrow-Band-Gap Particulate Photocatalysts for One-Step-Excitation Overall Water Splitting. *Acc. Chem. Res.* **2023**, *56* (7), 878−888.

(13) Sivula, K.; van de Krol, R. Semiconducting Materials for Photoelectrochemical Energy Conversion. *Nat. Rev. Mater.* **2016**, *1*, 15010.

(14) Osterloh, F. E. Inorganic Materials as Catalysts for Photochemical Splitting of Water. *Chem. Mater.* **2008**, *20* (1), 35−54.

(15) Osterloh, F. E. Inorganic Nanostructures for Photoelectrochemical and Photocatalytic Water Splitting. *Chem. Soc. Rev.* **2013**, *42* (6), 2294−2320.

(16) Hisatomi, T.; Kubota, J.; Domen, K. Recent Advances in Semiconductors for Photocatalytic and Photoelectrochemical Water Splitting. *Chem. Soc. Rev.* **2014**, *43* (22), 7520−7535.

(17) Wang, X. C.; Maeda, K.; Thomas, A.; Takanabe, K.; Xin, G.; Carlsson, J. M.; Domen, K.; Antonietti, M. A metal-free polymeric photocatalyst for hydrogen production from water under visible light. *Nat. Mater.* **2009**, *8* (1), 76−80.

(18) Maeda, K.; Teramura, K.; Saito, N.; Inoue, Y.; Domen, K. Photocatalytic overall water splitting on gallium nitride powder. *Bull. Chem. Soc. Jpn.* **2007**, *80* (5), 1004−1010.

(19) Zhou, P.; Navid, I. A.; Ma, Y.; Xiao, Y.; Wang, P.; Ye, Z.; Zhou, B.; Sun, K.; Mi, Z. Solar-to-hydrogen efficiency of more than 9% in photocatalytic water splitting. *Nature* **2023**, *613* (7942), 66−70.

(20) Shiga, Y.; Umezawa, N.; Srinivasan, N.; Koyasu, S.; Sakai, E.; Miyauchi, M. A metal sulfide photocatalyst composed of ubiquitous elements for solar hydrogen production. *Chem. Commun.* **2016**, *52* (47), 7470−7473.

(21) Taniguchi, Y.; Yoneyama, H.; Tamura, H. Hydrogen evolution on surface-modified silicon powder photocatalysts in aqueous ethanol solutions. *Chem. Lett.* **1983**, *12* (3), 269−272.

(22) Sato, J.; Saito, N.; Yamada, Y.; Maeda, K.; Takata, T.; Kondo, J. N.; Hara, M.; Kobayashi, H.; Domen, K.; Inoue, Y. RuO2-Loaded β-Ge3N4 as a Non-Oxide Photocatalyst for Overall Water Splitting. *J. Am. Chem. Soc.* **2005**, *127* (12), 4150−4151.

(23) Maeda, K.; Saito, N.; Lu, D.; Inoue, Y.; Domen, K. Photocatalytic Properties of RuO2-Loaded β-Ge3N4 for Overall Water Splitting. *J. Phys. Chem. C* **2007**, *111*, 4749−4755.

(24) Zhu, X.; Zhang, T.; Sun, Z.; Chen, H.; Guan, J.; Chen, X.; Ji, H.; Du, P.; Yang, S. Black Phosphorus Revisited: A Missing Metal-Free Elemental Photocatalyst for Visible Light Hydrogen Evolution. *Adv. Mater.* **2017**, *29* (17), 1605776.

(25) Ohmori, T.; Mametsuka, H.; Suzuki, E. Photocatalytic hydrogen evolution on InP suspension with inorganic sacrificial reducing agent. *Int. J. Hydrogen Energy* **2000**, *25* (10), 953−955.

(26) Bessekhouad, Y.; Mohammedi, M.; Trari, M. Hydrogen photoproduction from hydrogen sulfide on Bi2S3 catalyst. *Sol. Energy Mater. Sol. Cells* **2002**, *73* (3), 339−350.

(27) Madelung, O. *Semiconductors: Data Handbook.* 3rd ed.; Springer: Berlin, 2004; p 691.

(28) Chen, S.; Wang, L.-W. Thermodynamic Oxidation and Reduction Potentials of Photocatalytic Semiconductors in Aqueous Solution. *Chem. Mater.* **2012**, *24* (18), 3659−3666.

(29) Siddiqi, G.; Pan, Z.; Hu, S. Chapter Three—III-V Semiconductor Photoelectrodes. In *Semiconductors and Semimetals*; Mi, Z., Wang, L., Jagadish, C., Eds.; Elsevier, 2017; Vol. 97, pp 81−138.

(30) Ellis, A. B.; Bolts, J. M.; Kaiser, S. W.; Wrighton, M. S. Study of n-type gallium arsenide- and gallium phosphide-based photo-electrochemical cells. Stabilization by kinetic control and conversion of optical energy to electricity. *J. Am. Chem. Soc.* **1977**, *99* (9), 2848−2854.

(31) Hu, S.; Shaner, M. R.; Beardslee, J. A.; Lichterman, M.; Brunschwig, B. S.; Lewis, N. S. Amorphous TiO2 coatings stabilize Si, GaAs, and GaP photoanodes for efficient water oxidation. *Science* **2014**, *344* (6187), 1005−1009.

(32) Shen, X.; Zhao, T.; Su, H.; Yang, M.; Chen, J.; Liu, Y.; Yanagi, R.; Solanki, D.; Hu, S. Tuning Intermediate Bands of Protective Coatings to Reach the Bulk-Recombination Limit of Stable Water-Oxidation GaP Photoanodes. *Adv. Energy Mater.* **2022**, *12* (29), 2201314.

(33) Strandwitz, N. C.; Turner-Evans, D. B.; Tamboli, A. C.; Chen, C. T.; Atwater, H. A.; Lewis, N. S. Photoelectrochemical Behavior of Planar and Microwire-Array Si|GaP Electrodes. *Adv. Energy Mater.* **2012**, *2* (9), 1109−1116.

(34) Standing, A.; Assali, S.; Gao, L.; Verheijen, M. A.; van Dam, D.; Cui, Y.; Notten, P. H. L.; Haverkort, J. E. M.; Bakkers, E. P. A. M. Efficient water reduction with gallium phosphide nanowires. *Nat. Commun.* **2015**, *6*, 7824.

(35) Krawicz, A.; Cedeno, D.; Moore, G. F. Energetics and efficiency analysis of a cobaloxime-modified semiconductor under simulated air mass 1.5 illumination. *Phys. Chem. Chem. Phys.* **2014**, *16* (30), 15818−15824.

(36) Malizia, M.; Seger, B.; Chorkendorff, I.; Vesborg, P. C. K. Formation of a p-n heterojunction on GaP photocathodes for H2 production providing an open-circuit voltage of 710 mV. *J. Mater. Chem. A* **2014**, *2* (19), 6847−6853.

(37) Nozik, A. J. P-N Photoelectrolysis Cells. *Appl. Phys. Lett.* **1976**, *29* (3), 150−153.

(38) Halmann, M. Photoelectrochemical reduction of aqueous carbon dioxide on p-type gallium phosphide in liquid junction solar cells. *Nature* **1978**, *275* (5676), 115−116.

(39) Barton, E. E.; Rampulla, D. M.; Bocarsly, A. B. Selective solar-driven reduction of CO2 to methanol using a catalyzed p-GaP based photoelectrochemical cell. *J. Am. Chem. Soc.* **2008**, *130* (20), 6342−6344.

(40) Lee, S.; Bielinski, A. R.; Fahrenkrug, E.; Dasgupta, N. P.; Maldonado, S. Macroporous p-GaP Photocathodes Prepared by Anodic Etching and Atomic Layer Deposition Doping. *ACS Appl. Mater. Interfaces* **2016**, *8* (25), 16178−16185.

(41) Gronet, C. M.; Lewis, N. S. Design of a 13% efficient n-GaAs1-xPx semiconductor-liquid junction solar cell. *Nature* **1982**, *300* (5894), 733−735.

(42) Sun, J. W.; Liu, C.; Yang, P. D. Surfactant-Free, Large-Scale, Solution-Liquid-Solid Growth of Gallium Phosphide Nanowires and Their Use for Visible-Light-Driven Hydrogen Production from Water Reduction. *J. Am. Chem. Soc.* **2011**, *133* (48), 19306−19309.

(43) Zhao, Z.; Willard, E. J.; Dominguez, J. R.; Wu, Z.; Osterloh, F. E. Depletion layer controls photocatalytic hydrogen evolution with p-type gallium phosphide particles. *J. Mater. Chem. A* **2019**, *7* (30), 18020−18029.

(44) Garnett, E. C.; Yang, P. D. Silicon nanowire radial p−n junction solar cells. *J. Am. Chem. Soc.* **2008**, *130* (29), 9224−9225.

(45) Spitzer, W. G.; Gershenzon, M.; Frosch, C. J.; Gibbs, D. F. Optical absorption in n-type gallium phosphide. *J. Phys. Chem. Solids* **1959**, *11* (3−4), 339−341.

(46) Lacey, S. D. The absorption coefficient of gallium phosphide in the wavelength region 530 to 1100 nm. *Solid State Commun.* **1970**, *8* (14), 1115−1118.

(47) Dean, P. J.; Henry, C. H. Electron-Capture ("Internal") Luminescence from the Oxygen Donor in Gallium Phosphide. *Phys. Rev.* **1968**, *176* (3), 928−937.

(48) Kronik, L.; Shapira, Y. Surface Photovoltage Phenomena: Theory, Experiment, and Applications. *Surf. Sci. Rep.* **1999**, *37* (1−5), 1−206.

(49) Daemi, S.; Kaushik, S.; Das, S.; Hamann, T. W.; Osterloh, F. E. BiVO4-Liquid Junction Photovoltaic Cell with 0.2% Solar Energy Conversion Efficiency. *J. Am. Chem. Soc.* **2023**, *145* (47), 25797−25805.

(50) Cheng, Y.; Xiao, C.; Mahmoudi, B.; Scheer, R.; Maijenburg, A. W.; Osterloh, F. E. Effect of charge selective contacts on the quasi Fermi level splitting of CuGa3Se5 thin film photocathodes for hydrogen evolution and methylviologen reduction. *EES Catal.* **2023**, *1*, 74−83.

(51) Daemi, S.; Kundmann, A.; Becker, K.; Cendula, P.; Osterloh, F. E. Contactless measurement of the photovoltage in BiVO4 photo-electrodes. *Energy Environ. Sci.* **2023**, *16*, 4530−4538.

(52) Romanyuk, O.; Gordeev, I.; Paszuk, A.; Supplie, O.; Stoeckmann, J. P.; Houdkova, J.; Ukraintsev, E.; Bartoš, I.; Jiříček, P.; Hannappel, T. GaP/Si(0 0 1) interface study by XPS in combination with Ar gas cluster ion beam sputtering. *Appl. Surf. Sci.* **2020**, *514*, 145903.

(53) Mukherjee, J.; Erickson, B.; Maldonado, S. Physicochemical and Electrochemical Properties of Etched GaP(111)A and GaP(111)B Surfaces. *J. Electrochem. Soc.* **2010**, *157* (4), H487.

(54) Liu, Z.; Höfft, O.; Endres, F. Disproportionation Reaction of Gallium during Electrodeposition from an Ionic Liquid, Monitored by In Situ Electrochemical XPS. *J. Phys. Chem. C* **2021**, *125* (44), 24589−24595.

(55) Barr, T. L.; Klinowski, J.; He, H.; Albert, K.; Müller, G.; Lercher, J. A. Evidence for strong acidity of the molecular sieve cloverite. *Nature* **1993**, *365* (6445), 429−431.

(56) Doughty, R. M.; Hodges, B.; Dominguez, J.; Han, R.; Zhao, Z.; Assavachin, S.; Osterloh, F. E. Fermi Level Pinning Controls Band Bending and Photochemical Charge Separation in Particles of n-SrTiO3, n-SrTiO3:Al, and n-GaAs:Te. *J. Phys. Chem. C* **2020**, *124* (34), 18426−18435.

(57) Yang, Y.; Wang, J.; Zhao, J.; Nail, B. A.; Yuan, X.; Guo, Y.; Osterloh, F. E. Photochemical Charge Separation at Particle Interfaces: The n-BiVO4-p-Silicon System. *ACS Appl. Mater. Interfaces* **2015**, *7* (10), 5959−5964.

(58) Doughty, R. M.; Chowdhury, F. A.; Mi, Z.; Osterloh, F. E. Surface photovoltage spectroscopy observes junctions and carrier separation in gallium nitride nanowire arrays for overall water-splitting. *J. Chem. Phys.* **2020**, *153* (14), 144707.

(59) Sze, S. M. *Semiconductor Devices, Physics and Technology*, 2nd ed.; Wiley: New York, 2002; p 564.

(60) Dittrich, T. *Materials Concepts for Solar Cells*. Imperial College Press: London, 2015; p 516 (Page 197).

(61) Jakubec, I.; Vondrak, J.; Bludska, J.; Pekarek, L. Effect of the crystallographic orientation on photovoltaic properties of p-GaP electrodes. *Collect. Czech. Chem. Commun.* **1998**, *63* (1), 75−84.

(62) Popczun, E. J.; McKone, J. R.; Read, C. G.; Biacchi, A. J.; Wiltrout, A. M.; Lewis, N. S.; Schaak, R. E. Nanostructured Nickel Phosphide as an Electrocatalyst for the Hydrogen Evolution Reaction. *J. Am. Chem. Soc.* **2013**, *135* (25), 9267−9270.

(63) Trasatti, S. Work function, electronegativity, and electro-chemical behaviour of metals. *J. Electroanal. Chem.* **1972**, *39* (1), 163−184.

(64) McCrory, C. C. L.; Jung, S.; Ferrer, I. M.; Chatman, S. M.; Peters, J. C.; Jaramillo, T. F. Benchmarking Hydrogen Evolving Reaction and Oxygen Evolving Reaction Electrocatalysts for Solar Water Splitting Devices. *J. Am. Chem. Soc.* **2015**, *137* (13), 4347−4357.

(65) Maeda, K.; Teramura, K.; Lu, D. L.; Takata, T.; Saito, N.; Inoue, Y.; Domen, K. Characterization of Rh−Cr Mixed-Oxide Nanoparticles Dispersed on $(Ga_{1-x}Zn_x)(N_{1-x}O_x)$ as a Cocatalyst for Visible-Light-Driven Overall Water Splitting. *J. Phys. Chem. B* **2006**, *110* (28), 13753−13758.

(66) Yoshida, M.; Takanabe, K.; Maeda, K.; Ishikawa, A.; Kubota, J.; Sakata, Y.; Ikezawa, Y.; Domen, K. Role and Function of Noble-Metal/Cr-Layer Core/Shell Structure Cocatalysts for Photocatalytic Overall Water Splitting Studied by Model Electrodes. *J. Phys. Chem. C* **2009**, *113* (23), 10151−10157.

(67) Michaelson, H. B. Electron Work Function of the Elements. In *CRC Handbook of Chemistry and Physics*, 88 ed.; Lide, D. R., Ed. CRC Press/Taylor and Francis: Boca Raton, FL, 2008.

(68) Liu, X.; Li, B.; Wang, X.; Li, Y.; Zhao, J.; Li, Y.; Li, F. Enhanced Schottky Effect in the Ni2P Cocatalyst via Work Function Up-Shift Induced by MoO2 for Boosting Photocatalytic Hydrogen Evolution. *ACS Sustainable Chem. Eng.* **2022**, *10* (32), 10627−10640.

(69) Chassé, T.; Theis, W.; Chen, T. P.; Evans, D. A.; Horn, K.; Pettenkofer, C.; Jaegermann, W. Interface chemistry and band bending induced by Pt deposition onto GaP(110). *Surf. Sci.* **1991**, *251−252*, 472−477.

(70) Yang, Y.; Gu, J.; Young, J. L.; Miller, E. M.; Turner, J. A.; Neale, N. R.; Beard, M. C. Semiconductor interfacial carrier dynamics via photoinduced electric fields. *Science* **2015**, *350* (6264), 1061−1065.

(71) Mayer, J. M. Proton-coupled electron transfer: A reaction chemist's view. *Annu. Rev. Phys. Chem.* **2004**, *55*, 363−390.

(72) Osterloh, F. E. Photocatalysis versus Photosynthesis: A Sensitivity Analysis of Devices for Solar Energy Conversion and Chemical Transformations. *ACS Energy Lett.* **2017**, *2*, 445−453.

(73) Abe, R. Recent Progress on Photocatalytic and Photo-electrochemical Water Splitting under Visible Light Irradiation. *J. Photochem. Photobiol., C* **2010**, *11* (4), 179−209.

(74) Kumagai, H.; Minegishi, T.; Moriya, Y.; Kubota, J.; Domen, K. Photoelectrochemical Hydrogen Evolution from Water Using Copper Gallium Selenide Electrodes Prepared by a Particle Transfer Method. *J. Phys. Chem. C* **2014**, *118* (30), 16386−16392.

(75) Sasaki, Y.; Nemoto, H.; Saito, K.; Kudo, A. Solar Water Splitting Using Powdered Photocatalysts Driven by Z-Schematic Interparticle Electron Transfer without an Electron Mediator. *J. Phys. Chem. C* **2009**, *113* (40), 17536−17542.

(76) Chen, S.; Vequizo, J. J. M.; Pan, Z.; Hisatomi, T.; Nakabayashi, M.; Lin, L.; Wang, Z.; Kato, K.; Yamakata, A.; Shibata, N.; Takata, T.;

Yamada, T.; Domen, K. Surface Modifications of (ZnSe)0.5-(CuGa2.5Se4.25)0.5 to Promote Photocatalytic Z-Scheme Overall Water Splitting. *J. Am. Chem. Soc.* **2021**, *143* (28), 10633−10641.

(77) Buehler, N.; Meier, K.; Reber, J. F. Photochemical Hydrogen-Production with Cadmium-Sulfide Suspensions. *J. Phys. Chem.* **1984**, *88* (15), 3261−3268.

(78) Huang, Y. C.; Zhang, Z. C.; Jiang, H. Y. Photocatalytic Properties of Pt/GaP Nanoparticles under Visible Light Irradiation. *J. Inorg. Mater.* **2011**, *26* (6), 579−584.

(79) Dang, H. V.; Wang, Y. H.; Wu, J. C. S. Exploration of photocatalytic seawater splitting on Pt/GaP-C3N4 under simulated sunlight. *Appl. Surf. Sci.* **2022**, *572*, 151346.

(80) Dang, H. V.; Wang, Y. H.; Wu, J. C. S. Z-scheme photocatalyst Pt/GaP-TiO2-SiO2:Rh for the separated H2 evolution from photocatalytic seawater splitting. *Appl. Catal., B* **2021**, *296*, 120339.

(81) Meek, R. L.; Schumaker, N. E. Anodic Dissolution and Selective Etching of Gallium Phosphide. *J. Electrochem. Soc.* **1972**, *119* (9), 1148.

(82) Memming, R.; Schwandt, G. Electrochemical properties of gallium phosphide in aqueous solutions. *Electrochim. Acta* **1968**, *13* (6), 1299−1310.

(83) Cao, S.; Chen, Y.; Wang, C.-J.; He, P.; Fu, W.-F. Highly efficient photocatalytic hydrogen evolution by nickel phosphide nanoparticles from aqueous solution. *Chem. Commun.* **2014**, *50* (72), 10427−10429.

(84) Maeda, K.; Teramura, K.; Masuda, H.; Takata, T.; Saito, N.; Inoue, Y.; Domen, K. Efficient Overall Water Splitting under Visible-Light Irradiation on $(Ga_{1-x}Zn_x)(N_{1-x}O_x)$ Dispersed with Rh−Cr Mixed-Oxide Nanoparticles: Effect of Reaction Conditions on Photocatalytic Activity. *J. Phys. Chem. B* **2006**, *110* (26), 13107−13112.